Artificial graphene in a strong magnetic field:
Bulk current distribution and quantum phase transitions

Z. E. Krix ⊙* and O. P. Sushkov ⊙

School of Physics, University of New South Wales, Sydney 2052, Australia

We present calculations of the equilibrium current density and Chern numbers for a two-dimensional electron gas in a sinusoidal periodic potential with infinite strip geometry and a perpendicular magnetic field. We consider a triangular lattice of antidots with large ($a = 120$ nm) lattice spacing. Such a system is known as artificial graphene (AG). To compute the current density we numerically diagonalize the AG Hamiltonian over a set of Landau level basis states; this takes into account coupling between different Landau levels. Our calculations show that, at magnetic fields typical for quantum Hall measurements, extended streams of current are present in the bulk of the sample when the chemical potential lies within a bulk band gap. We investigate the scaling of these streams with potential strength. Knowledge of the AG energy levels allows us to compute the Chern number associated with each energy gap. We demonstrate that in tuning the height of the potential modulation the Chern number can undergo a transition between two different values.

I. INTRODUCTION

Artificial graphene (AG) is intended to simulate the electronic properties of graphene. The simulation must be controllable, including the possibility of switching on the spin-orbit interaction. Such systems can be realized by imposing a supermodulation with triangular lattice symmetry on a two-dimensional gas of particles since this symmetry necessarily gives rise to Dirac cones. Artificial triangular arrays (superlattices) have been realized in semiconductor quantum wells with strong [1–3] and weak [4,5] modulation, in twisted bilayer graphene [6,7], and in optical lattices of cold atoms [8,9]. For a review see Ref. [10].

In the current work, we consider, theoretically, AG produced via electrostatically gated GaAs quantum wells with repulsive lattice sites and typical lattice constants of the order of 100 nm. In principle, the band structure of such a system should exhibit two sets of Dirac cones and a topological flat band [11]. The latter work has established that arrays of antidots (when produced electrostatically) are less susceptible to disorder than arrays of dots. Due to the layered structure and due to the low energy scale, spectroscopic methods such as ARPES are not applicable to these devices. Therefore, signatures of the superlattice potential are sought in transport measurements. More information can be obtained from transport properties when a perpendicular magnetic field is present and R_{xx} and R_{xy} are measured as functions of this field.

The problem of electron dynamics in a superimposed magnetic field and periodic potential has been considered in numerous works. However, previously this problem was considered in the weak modulation limit, with the amplitude of the potential modulation much lower than the electron

Fermi energy. For example, in the experiment by Geisler *et al.* [4] the modulation amplitude was just a few percent of the Fermi energy. Theoretically, the weak modulation limit is addressed in Refs. [12–16]. However, for AG one needs the amplitude of the potential modulation to be several times higher than the Fermi energy [11], and this case has not been considered before in a magnetic field. It is important to stress that we address the case where the periodic potential is produced by electrostatic gating. This always results in a sinusoidal potential. AG corresponds to a regime that we call a moderate potential strength to distinguish it from the case of infinite antidots. A sinusoidal potential of very high amplitude does not produce Dirac cones. Moderately strong potentials can be addressed only numerically, and in the present work we perform such a calculation considering an infinite stripe of a finite width. The finite width is necessary to address the edge states. In this work we perform calculations of the Hall conductivity and current density in the bulk bandgaps of a triangular lattice system with a perpendicular magnetic field. The regime which we consider is directly relevant to experimental work in progress [17] on AG in GaAs quantum wells.

In our work we observe two qualitatively new effects. (i) Proper variation of the potential amplitude drives topological phase transitions between states with different Chern numbers. Hence, the sequence of quantum Hall plateaus of R_{xy} depends on the modulation amplitude and we predict this dependence. (ii) The superlattice generates bulk current streams when the chemical potential lies within a bulk bandgap. The effect cannot be observed in standard terminal measurements, but it can be observed using nitrogen-vacancy-center magnetometry.

The structure of the paper is the following: In Sec. II we discuss the details of our calculation. Section III addresses the structure of bulk bands and the edge states. In Sec. IV we discuss the Hall conductivity and density of states for the

---

*z.krix@unsw.edu.au

case with a high density of bulk bands. Section V presents a map of the Hall conductivity. Quantum phase transitions are considered in Sec. VI, and streams of current in the bulk are demonstrated in Sec. VII.

II. MATRIX ELEMENTS OF THE HAMILTONIAN AND CALCULATION TECHNIQUES

The general approach used is the same as that in Refs. [13,15]: A single-particle Hamiltonian with a triangular lattice potential is diagonalized over the basis of Landau level eigenvectors. We extend the calculation by computing the matrix elements of the Hamiltonian for arbitrary Landau levels and by allowing transitions between them. A further extension is the addition of a confining potential $V(x)$ which defines the edges of the sample along the x direction. This, together with periodic boundary conditions along the y direction, imposes a strip geometry with a very high aspect ratio (Fig. 1).

While the matrix elements of the lattice Hamiltonian can be computed exactly, the matrix elements of the confining potential must be computed via numerical integration. We can then numerically diagonalize this matrix to obtain energy levels (in the form of a dispersion relation) and eigenvectors. The remainder of this section clarifies some of the details of this process.

Landau level eigenstates in the gauge $\boldsymbol{A} = (0, Bx, 0)$ are given by

$$
\psi_{k,n}(x, y) = A_n e^{iky} e^{-\xi^2/2} H_n(\xi),
$$
$$
A_n = \frac{1}{\sqrt{2^n n!}} \left(\frac{m\omega}{\pi} \right)^{1/4}, \tag{1}
$$

where k is the momentum along the length of the stripe, $x_k = k/eB$ is the center coordinate, and $\xi = (x - x_k)/l_B$ is

the position in units of the magnetic length ($l_B = 1/\sqrt{eB}$). The functions $H_n(\xi)$ are the Hermite polynomials. The single-particle Hamiltonian is given by $H = \boldsymbol{p}^2/2m + U(\boldsymbol{r})$ with

$$
U(\boldsymbol{r}) = 2W \sum_{i=1}^{3} \cos(\boldsymbol{g}_i \cdot \boldsymbol{r}) \tag{2}
$$

for reciprocal lattice vectors g_i,

$$
\boldsymbol{g}_1 = g_0(1/2, \sqrt{3}/2),
$$
$$
\boldsymbol{g}_2 = g_0(1, 0),
$$
$$
\boldsymbol{g}_3 = g_0(-1/2, \sqrt{3}/2),
$$
$$
g_0 = 2g/\sqrt{3}, \quad g = 2\pi/a. \tag{3}
$$

We wish to compute the matrix elements,

$$
\langle k_i, n|H|k_j, m \rangle = \delta_{nm} \delta_{ij} \omega_c (n + 1/2)
$$
$$
+ \iint \bar{\psi}_{k_i,n}(\boldsymbol{r} - x_{k_i}) \psi_{k_j,m}(\boldsymbol{r} - x_j)
$$
$$
\times (U(\boldsymbol{r}) + V(x)) dx dy,
$$

with $\psi_{k,n}(\boldsymbol{r})$ given in Eq. (1). The integral over $U(\boldsymbol{r})$ can be evaluated analytically for arbitrary n, m. To do this we first write the potential, (2), in an alternate form,

$$
U(\boldsymbol{r}) = 2W \cos(g_0 x) + 4W \cos(gy) \cos(g_0 x/2). \tag{4}
$$

The first of these terms is diagonal in y momentum and the second is strictly off-diagonal in y momentum, only mixing those states whose momenta are separated by $\pm g$. Performing the integration gives the following form for the matrix elements of U:

$$
\langle k_i, n|\hat{U}|k_j, m \rangle = 2W \delta_{ij} X_{nm}(k_i) + 2W \delta(k_i - k_j \pm g) \big[\cos(g_0 x_k/2) F_{nm}^{(1,\pm)} + \sin(g_0 x_k/2) F_{nm}^{(2,\pm)} \big], \tag{5}
$$

where these two terms correspond to the two terms in Eq. (4), respectively. We find the following equations for the matrices $X(k)$ and $F^{(i,\pm)}$:

$$
X_{nm}(k) = \begin{cases} (-1)^{(m-n)/2} \cos(g_0 x_k) \\ \quad \times \frac{\sqrt{2^n n!}}{\sqrt{2^m m!}} (g_0 l_B)^{m-n} e^{-(g_0 l_B)^2/4} L_n^{m-n} ((g_0 l_B)^2/2), \quad m+n \text{ even}, \\ (-1)^{(m-n-1)/2} \sin(g_0 x_k) \\ \quad \times \frac{\sqrt{2^n n!}}{\sqrt{2^m m!}} (g_0 l_B)^{m-n} e^{-(g_0 l_B)^2/4} L_n^{m-n} ((g_0 l_B)^2/2), \quad m+n \text{ odd}, \end{cases} \tag{6}
$$

$$
F_{nm}^{i,\pm} = A_n A_m e^{-\xi_g^2/2} \sum_{r,p=0}^{n,m} \binom{n}{r} \binom{m}{p} (\mp \xi_g)^r (\pm \xi_g)^p (A_{n-r} A_{m-p})^{-1} X_{n-r,m-p}(G_i)\big|_{g_0 \mapsto g_0/2}, \tag{7}
$$

where L_n^{m-n} are the associated Laguerre polynomials and $\xi_g = x_{k=g}/l_B$ (the center coordinate in units of magnetic length). In the second equation [Eq. (7)] we have used the notation $G_{i=1} = \pm g/2$ and $G_{i=2} = \pm g/2 + \pi eB/g_0$. We have written the matrix $F^{i,\pm}$ in terms of X [Eq. (6)], with g_0 replaced everywhere by $g_0/2$. In the limit of small coupling between Landau levels, setting $n = m = 0$ reduces the Hamiltonian to that given by MacDonald [15].

What remains is to compute the matrix elements of the confining potential $V(x)$, which defines the edges of the sample.

We define $V(x)$ in terms of the Heaviside step function $\theta(x)$:

$$
V(x) = E_0 \theta(|x| - L_x/2). \tag{8}
$$

The sample geometry imposed by this edge potential is sketched in Fig. 1.

In order to obtain a numerical solution for the energy levels we need to consider a finite value of E_0. The precise value of E_0 is not important but it must be chosen such that the height of the edge potential is well above the energy of any of the states considered in this work. In addition to this constraint,
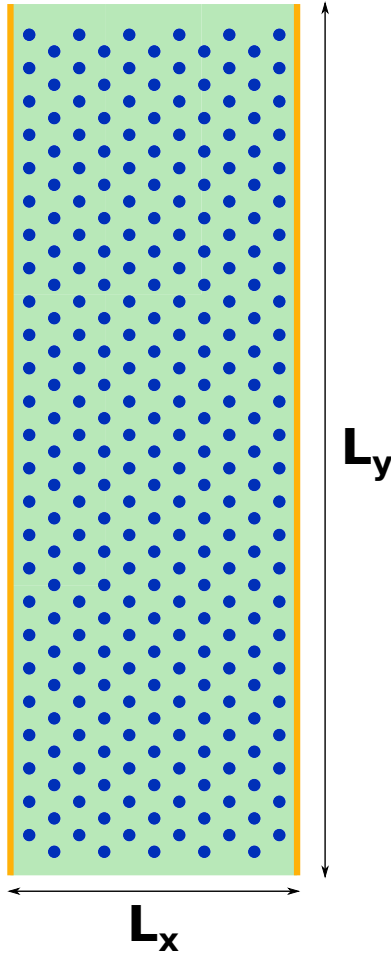
FIG. 1. A long stripe of width $L_x = 10a$ used in the calculations, $L_y \gg L_x$.

E_0 cannot be too large since larger values of E_0 require a larger number of basis vectors. For the purposes of this calculation we set $E_0 = 30$ meV and $L_x = 10a$ or $30a$, where $a = 120$ nm is the lattice constant. Matrix elements, (9), of the confining potential cannot be computed analytically. We therefore perform the integration numerically:

$$\langle k, n|V|k, m \rangle = E_0 \int_{-\infty}^{x_k - L_x/2} \bar{\psi}_{k,n}(\mathbf{r})\psi_{k,m}(\mathbf{r})dxdy$$

$$+ E_0 \int_{x_k + L_x/2}^{\infty} \bar{\psi}_{k,n}(\mathbf{r})\psi_{k,m}(\mathbf{r})dxdy. \quad (9)$$

This completes our calculation of the Hamiltonian matrix.

With the Hamiltonian given we can numerically diagonalize this matrix to obtain all energy levels and eigenstates. The energy levels evolve with magnetic field in the well-known Hofstadter butterfly pattern [12], with corrections due to having a triangular lattice (as opposed to a square one) and due to inter-Landau-level coupling.

For the sake of convenience we measure the magnetic field by the number of flux quanta per lattice unit cell. The flux quantum [18] is $\phi_0 = h/e$ and the flux per unit cell is

$\phi = Ba^2 \frac{\sqrt{3}}{2}$. For the lattice spacing $a = 120$ nm that we consider,

$$\phi = \phi_0 \quad \text{corresponds to} \quad B = 0.332 \text{ T}. \quad (10)$$

The Hofstadter butterfly has a fractal structure. This band structure is simple when the flux is a rational number:

$$\frac{\phi}{\phi_0} = \frac{p}{q}. \quad (11)$$

In this case each Landau level is split into p subbands [13].

In addition to the energy levels, numerical diagonalization of the Hamiltonian gives a set of eigenstates $\psi_{\lambda,k}(\mathbf{r})$, where λ enumerates energy bands of the combined magnetic field and superlattice system and k is the y momentum modulo g. As soon as the eigenstates are known we can compute the electric current:

$$j_{x,y} = \frac{ei}{2m} \sum_{\epsilon_\lambda(k) < \mu} (\psi_{\lambda,k}^\dagger(\mathbf{r})[\partial_{x,y} + ieA_{x,y}]\psi_{\lambda,k}(\mathbf{r})$$

$$- \psi_{\lambda,k}(\mathbf{r})[\partial_{x,y} + ieA_{x,y}]\psi_{\lambda,k}^\dagger(\mathbf{r})). \quad (12)$$

To find the total current density we sum the contributions due to individual quantum states $\psi_{\lambda,k}(\mathbf{r})$ below the chemical potential [i.e., $\psi_{\lambda,k}(\mathbf{r})$ such that $\epsilon_\lambda(k) < \mu$, where μ is the chemical potential]. In practice we compute only the y component of the current density, (12), from the eigenstates and evaluate the x component using the continuity equation:

$$\partial_x j_x + \partial_y j_y = 0 \Rightarrow j_x(x, y) = \int_{-\infty}^{x} \partial_y j_y(x, y)dx.$$

Finally, this work also covers the Hall conductivity. It is well known that the Hall conductivity within a bulk bandgap is determined by the edge states and is hence universal [19]. Inside bulk bands the Hall conductivity is not universal; it depends on the disorder. In this work we are interested only in the universal properties of the system and we can calculate the Hall conductivity and corresponding Chern numbers by manually counting the edge states. This method, discussed in the following section, is efficient when the flux takes on simple rational values. However, it becomes difficult at values of the flux for which the number of energy gaps is large. It is also impractical to manually count edge modes over a range of many magnetic fields. Computationally it is more efficient to use the Streda equation [20,21],

$$\sigma_{xy}^{(q)} = e\frac{\partial n_s}{\partial B}, \quad (13)$$

where n_s is the total electron density and the derivative is taken at a constant chemical potential. It is important to note that this equation does not give the total Hall conductivity. As detailed in Ref. [21] there are two terms which contribute to σ_{xy}: a quantum term, which is given in Eq. (13), and a 'classical' term. The classical term corresponds to electron drift and is nonzero only within a bulk subband. In Eq. (13) we include only the quantum term and stress this point by adopting the notation $\sigma_{xy}^{(q)}$. Equation (13) is thus only valid when the chemical potential is within a bulk bandgap.

In Eq. (13) we calculate n_s numerically by directly counting the number of states below a fixed chemical potential. We vary the magnetic field in steps of $d\phi = 2 \times 10^{-3}\phi_0$. We find
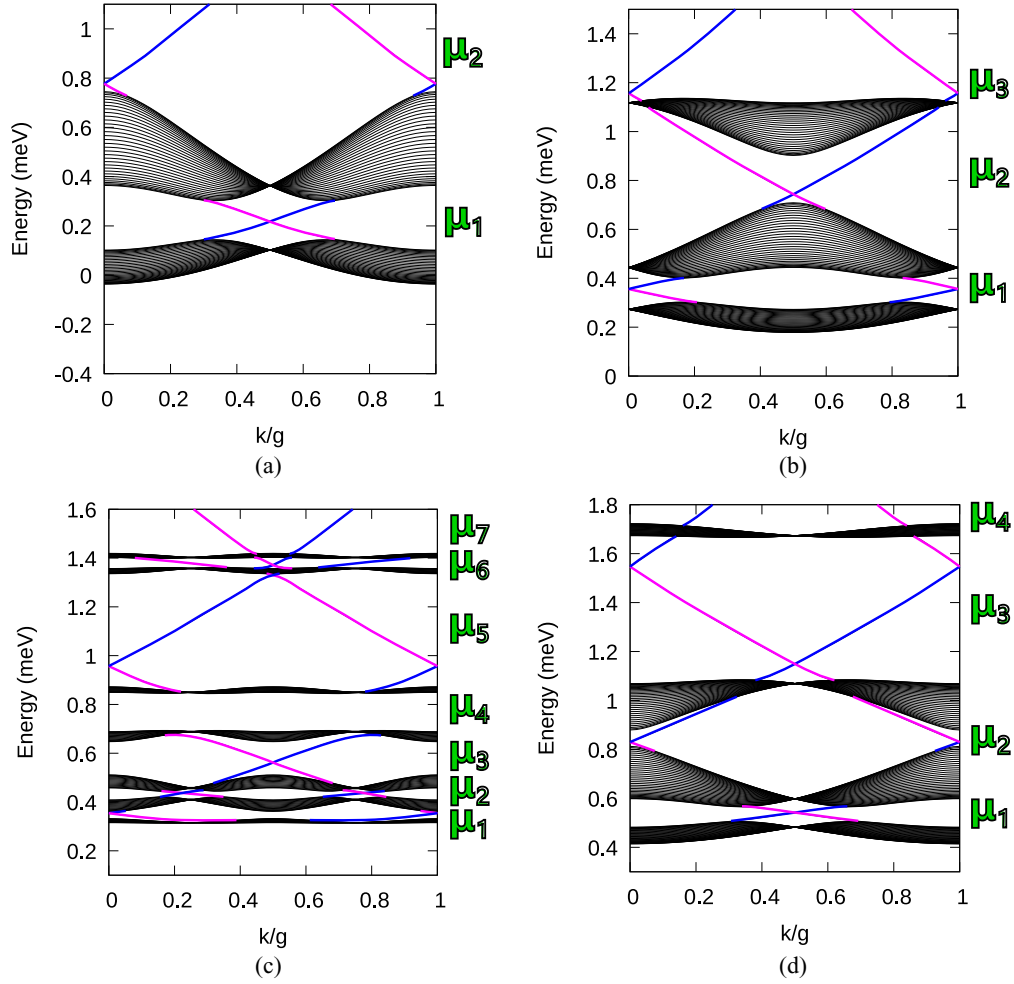
FIG. 2. Calculated dispersions within the $n = 0$ Landau level for the following values of magnetic flux: (a) $\phi/\phi_0 = 2$ (two subbands), (b) $\phi/\phi_0 = 3$ (three subbands), (c) $\phi/\phi_0 = 7/2$ (seven subbands), and (d) $\phi/\phi_0 = 4$ (four subbands). The potential strength is $W = 0.4$ meV and the sample width is $L_x = 30a$ for a superlattice period $a = 120$ nm. The edge-state dispersions are shown in color, with the left edge blue and the right edge magenta.

that large values of $\sigma_{xy}^{(q)}$ computed using Eq. (13) correspond to regions with a high density of bandgaps. Therefore, we also use Eq. (13) to "truncate" the fractal map of the Chern number over the (μ, ϕ) plane. We discuss this truncation procedure in further detail below.

Within a bandgap it is generally true that

$$\sigma_{xy} = 2\nu \frac{e^2}{h}, \qquad (14)$$

where ν is an integral Chern number. The factor 2 is for spin degeneracy, which we assume throughout this work.

To reiterate, Eq. (13) is completely equivalent to counting the edge modes by hand. It is more convenient for computations to use Eq. (13).

III. BAND STRUCTURES AND EDGE STATES

In this section we aim to demonstrate how our technique works. We do not present any qualitatively new results. Previously, similar calculations have been performed for the case of a weak square-lattice potential [22].

Our calculations, shown in Fig. 2, were performed at $W = 0.4$ meV. The bandwidth of this potential is

$$\Delta E = 9W = 3.6 \text{ meV.} \qquad (15)$$

For a magnetic field $B = 1$ T the cyclotron frequency in GaAs is $\hbar\omega = 1.74$ meV and the capacity of a single Landau level (including spin degeneracy) is $n_L = 2\frac{B}{\phi_0} = 0.48 \times 10^{11}$ cm^{-2}. Without a magnetic field this density would correspond to a Fermi energy $\epsilon_F = 1.74$ meV. Both $\hbar\omega$ and ϵ_F are significantly smaller than the bandwidth [Eq. (15)]. Previous work [11] has shown that at this potential a set of Dirac cones is present at a low density ($n_s = 1.6 \times 10^{10}$ cm^{-2}). A potential that is several times stronger is required to observe a second pair of Dirac cones at a higher density ($n_s = 6.4 \times 10^{10}$ cm^{-2}).

In Fig. 2 we present calculated dispersions for the split lowest Landau level at $\phi/\phi_0 = 2, 3, 7/2$, and 4. These values of flux correspond to $B = 0.663, 0.995, 1.160$, and 1.326 Tesla. From these figures it can be seen that the number of subbands is equal to the numerator of ϕ/ϕ_0.

For each case in Fig. 2 the effective width of the $n = 0$ Landau level is about 1 meV. The lowest subband of the $n = 1$ Landau level (not shown in Fig. 2) is about 1 meV above the topmost subband of the $n = 0$ Landau level. Thus the effective width of the Landau level is comparable to the separation between the levels.

The dispersions in Fig. 2 consist of dense subbands of bulk states with edge states in "gaps" between the subbands. Since we know the wave functions we know to which edge, left or right, the edge state belongs (see Fig. 1). In Fig. 2 the left edge dispersions are shown in blue and the right ones in magenta. Counting, say, the left edge states one can find the Chern number in Eq. (14): in a given gap every left edge state with a positive slope gives $\Delta\nu = 1$, and every left edge state with a negative slope gives $\Delta\nu = -1$. Hence the sequences of Chern numbers corresponding to the labeled chemical potential values in Fig. 2 are the following: Fig. 2(a), 1, 1; Fig. 2(b), 1, 1, 1; Fig. 2(c), 1, 2, 1, 0, 1, 2, 1; and Fig. 2(d), 1, 1, 1, 1.

IV. DENSITY OF STATES AND HALL CONDUCTIVITY AT A HIGH DENSITY OF SUBBANDS

Here we comment on the statement that $\phi/\phi_0 = p/q$ implies that there are p subbands—and what that means when the flux is not a simple rational number. The purpose of this discussion is to provide a background for understanding the maps of Hall conductivity which we present in the following sections.

Because of the fractal nature of the Hofstadter butterfly it is instructive to see how the band structure changes in the vicinity of $\frac{\phi}{\phi_0} = \frac{p}{q}$. In Fig. 3 we plot the Hall conductivity [23] (black) and the density of states [24] (red) as a function of the energy and consider fields close to three flux quanta. The Hall conductivity is computed using Eq. (13) and the density of states is given in arbitrary units. Figures 3(a) and 3(b) correspond to $\frac{\phi}{\phi_0} = 3$ [as in Fig. 2(b)], while Figs. 3(c) and 3(d) correspond to $\frac{\phi}{\phi_0} = 2.96 = \frac{74}{25}$.

Figure 3(a) shows clearly that there are three subbands. In the gaps between bulk bands when the density of states goes to 0, the total Hall conductivity is $\sigma_{xy} = 2e^2/h$. Inside the bands $\sigma_{xy}^{(q)}$ and the density of states take some fluctuating values. The fluctuations in the density of states are due to confinement along the x axis. Calculated values of $\sigma_{xy}^{(q)}$ inside the bands are not the total Hall conductivity and, hence, could be unphysical.

Small changes in the magnetic field give a dramatic change in the numerator of ϕ/ϕ_0. Figure 3 illustrates how this is possible. A change in the field of around 1% from Fig. 3(a) to Fig. 3(c) changes the expected number of subbands from 3 to 74 (and the number of energy gaps from 2 to 73). While this is true, the broad gaps in Figs. 3(a) and 3(c) are almost identical. The new narrow gaps in Fig. 3(c) "arise" from the continuous spectrum in Fig. 3(a). In this sense there is some "continuity" in the fractal butterfly.

In addition to the broad plateaus in Fig. 3(d) there is also some finer structure. For example, there is a plateau, $\nu = 0$, at $\mu = 0.9$ meV. The plateau immediately next to this is $\nu = -1$. Beyond this the plateaus become poorly quantized
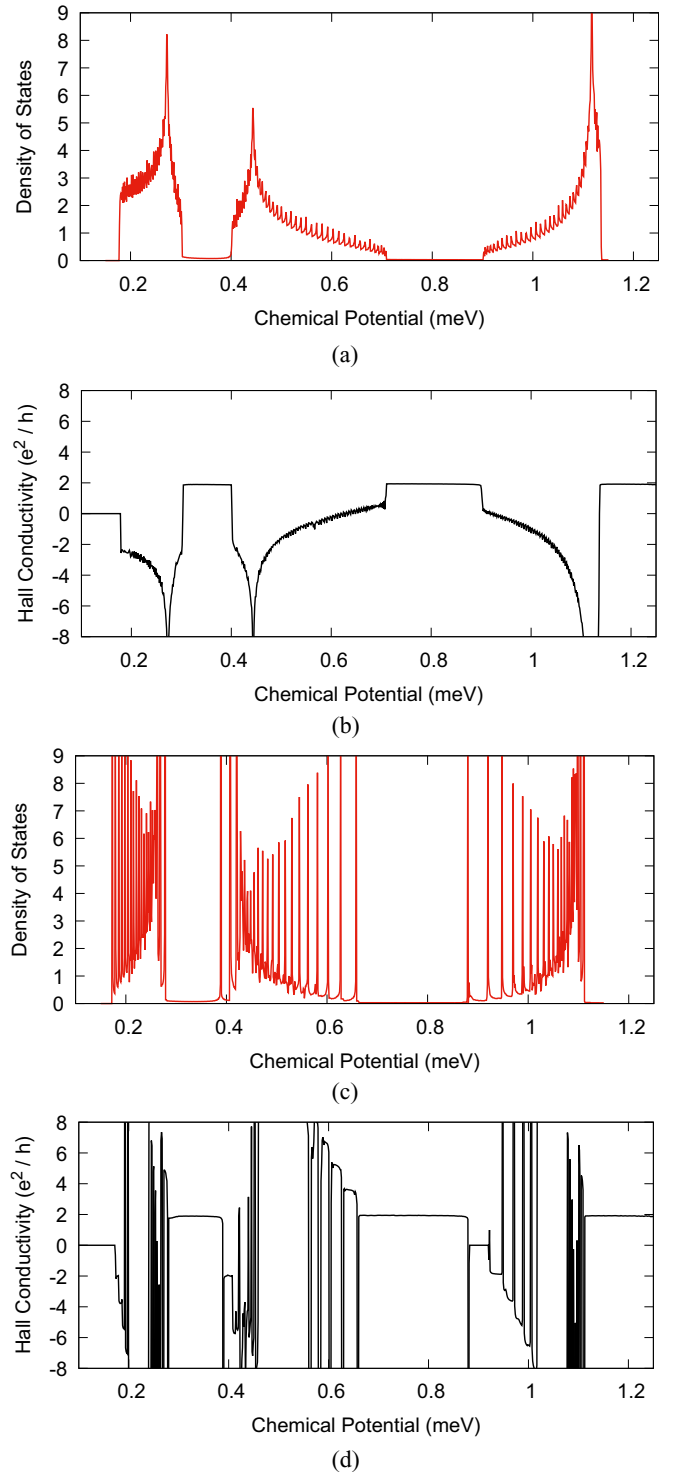

(a)

(b)

(c)

(d)

FIG. 3. Density of states as a function of the chemical potential for (a) $\phi/\phi_0 = 3$ and (c) $\phi/\phi_0 = 2.96$, given in arbitrary units. Hall conductivity as a function of the chemical potential for (b) $\phi/\phi_0 = 3$ and (d) $\phi/\phi_0 = 2.96$, computed using Eq. (13). As in Fig. 2 we have $W = 0.4$ meV and $L_x = 30a$. The Hall conductivity is computed via Eq. (13), which is valid within energy gaps (see discussion at the end of Sec. II).

with $\nu \approx -2$, -3, etc. (see also the plateaus around $\mu = 0.6$ meV). Nonquantization of σ_{xy} in the small energy gaps is most likely due to our use of a finite sample size. Please

note that the negative values of ν that we observe (e.g., near $\mu = 0.4$ and 0.9 meV) are physical. They correspond to the existence of edge modes which travel in the direction opposite to that of a standard skipping orbit around the sample boundary. These states can be visualized as skipping orbits traveling along antidots close to the edge.

Finally, there is a limit to the maximum number of subbands a Landau level can split into. Consider the effect of a finite sample size on the Hofstadter butterfly fractal structure. Once a finite sample width has been defined there is a limit on the maximum number of subbands that can be resolved (e.g., close to an integer flux). This limit is equal to the number of energy bands (Λ) in a single Landau level. If N is the total number of states within a Landau level, then

$$N = n_s L_x L_y = 2\Lambda g L_y / 2\pi$$

$$= 2B L_x L_y / \phi_0$$

$$\Rightarrow \Lambda = B L_x a / \phi_0, \tag{16}$$

where we have used the fact that a single energy band contains a number of states equal to $2\int dk L_y / 2\pi = 2g L_y / 2\pi = 2L_y/a$. In the case in Fig. 3 with $L_x = 30a$, Eq. (16) gives $\Lambda = 104$. The implication is that all subbands in Figs. 3(a) and 3(c) should be resolvable, while at fluxes closer to $\phi/\phi_0 = 3$ (which have larger numbers of subbands) the finer structure of the Hofstadter butterfly will be not be resolved. While we have this theoretical limit to the number of subbands (at ϕ close to 3) it may still be impossible to resolve all of the subbands, even when $p < \Lambda$. In Fig. 3(c) some of the energy gaps are still too small to distinguish two bulk bands, hence a counting of the bands gives around 70. In these ways some of the fine structure in the spectrum is removed. Disorder will also introduce a broadening of the density of states which also obscures details of the fractal structure.

V. HALL CONDUCTIVITY MAP

We now present (in Fig. 4) the map of σ_{xy} over the flux-energy plane. We perform this calculation using Eq. (13) as in Figs. 3(b) and 3(d). Strictly speaking a fractal function cannot be mapped because all features in the spectrum that are smaller than some energy scale will not be represented. However, due to disorder and a finite sample size, the Hofstadter butterfly of any real sample will not be a true fractal.

Since Eq. (13) is not valid within bulk subbands, we wish to eliminate points in Fig. 4 which correspond to bulk states. We thus show all states with μ inside a bulk band or a region with a high density of bulk bands in black [as in Fig. 3(d)]. We do this by comparing the map of Hall conductivity to the computed band structure over the same region of the (μ, B) plane. This coloring highlights the large continuous energy gaps in the uniform Chern number with which we are concerned in this work. These features are 'robust' in the sense that they are not changed by the presence or type of disorder. Hall conductivity within bulk bands is device dependent and this nonuniversal behavior is not within the scope of this work.

Thus, Fig. 4 shows the Hall conductivity of only the largest energy gaps in color and shows the bulk subbands of the Hofstadter butterfly in black. We make predictions for the
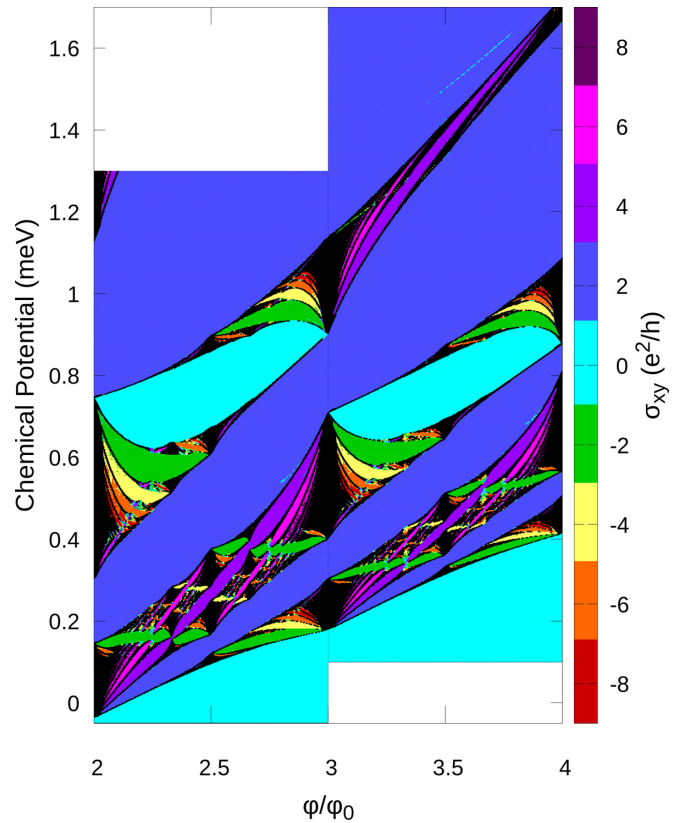

FIG. 4. Color map of σ_{xy} computed numerically using Eq. (13) plotted as a function of the chemical potential and flux per unit cell. As in Fig. 2(b) the potential strength is $W = 0.4$ meV and only the lowest Landau level is shown.

sequence of σ_{xy} values at arbitrary fields in the range $\phi/\phi_0 \in [2, 4]$. For example, we compute the following sequences (in units of e^2/h): at $\phi/\phi_0 = 5/2$, $\sigma_{xy} = 2, 4, 2, 0, 2$; at $\phi/\phi_0 = 8/3 = 2.\dot{6}$, $\sigma_{xy} = -2, 2, 6, 4, 2, 0, -2$; and at $\phi/\phi_0 = 10/3 = 3.\dot{3}$, $\sigma_{xy} = 2, -2, 6, 2, -2, 0, 2, 4, 6, 2$. Previous work by MacDonald [15] has computed these sequences in the small-W limit and in the highly anisotropic limit [here, anisotropic means that the second term in the potential, (4), is much smaller than the first]. At small W there are discrepancies with our results due to the change from an anisotropic to an isotropic lattice. For example, the second gap at $\phi/\phi_0 = 7/3$ from -2 to 4 changes during this transition. At the values of W we consider (where first-order perturbation theory is no longer applicable) there are additional discrepancies. For example, the fourth gap at $\phi_0/\phi_0 = 8/3$ is 4 in our calculation and -2 in Ref. [15]. There are also differences between our calculations and the weak potential calculation that occur in larger energy gaps. This is discussed in the next section.

All of the values for $\sigma_{xy} = 2\nu e^2/h$ that we observe are solutions to the Diophantine equation introduced by Thouless *et al.* [14]. If i is the energy gap index ($i = 1, 2, \ldots, p$), $\phi/\phi_0 = p/q$, and w is an arbitrary integer, then

$$i = p\nu + qw \tag{17}$$

for every gap we observe. For example, in gap 1 at $\phi/\phi_0 = 5/2$ we find $\nu = 1$ (Fig. 4). Equation (17) is satisfied with $\nu = 1$ and $w = -2$: $1 = 5 \times 1 + 2 \times (-2)$. In this case Eq. (17)

forbids solutions $\nu = 0, \pm 2, \pm 4, \ldots$ since increasing $\nu = 1$ by unity would give an odd change to the first term which cannot be canceled by the second term (which is even).

It is relevant to the results below that different integer solutions ν to the above equation are separated by q: Given some solution (ν, w) to Eq. (17) we can write $\nu = (i - qw)/p$. A second integer solution, (ν', w'), can then be obtained by taking $w' = w - p$ so that $\nu' = \nu + q$.

While our results conform to Eq. (17) we cannot use (17) to predict σ_{xy} in an arbitrary energy gap. To make predictions using (17) there needs to be a restriction on the values w so that (17) has a unique solution. So far this has only been achieved for a weak triangular lattice in the anisotropic limit [15]. Our calculation, in addition to predicting the sequence of σ_{xy} values in a moderately strong potential, also gives the relative sizes of the energy gaps and shows which gaps are connected by a continuous region of edge states.

Illustration of the Streda equation

As an illustration of Eq. (13) consider the following example. When the chemical potential μ is in an energy gap between two Landau levels [μ_3 in Fig. 2(b)] the number of states below μ is just an integer multiple, ν, of the Landau degeneracy factor $n_L = 2B/\phi_0$. Thus, $n_s = 2e\nu B/h$. Computing σ_{xy} via Eq. (13) gives $\sigma_{xy} = 2\nu e^2/h$, an integer multiple of e^2/h as expected. For energy gaps *inside* a Landau level [e.g., μ_1 and μ_2 in Fig. 2(b)] the calculation can similarly be done by hand.

Figure 4 shows the function $\sigma_{xy}(\mu, B)$ computed via Eq. (13), with n_s obtained from the set of energy levels that come out of the numerical diagonalization procedure. Since the density of states is dominated by bulk states this can be considered a bulk calculation. This figure (in addition to showing σ_{xy}) illustrates the evolution of the spectrum as the magnetic field is varied. For example, it can be seen that at $\phi/\phi_0 = 2, 3$, and 4 there are two, three, and four subbands, respectively. As an example of how Eq. (13) works *within* a Landau level consider the gap in Fig. 4, which continuously stretches from gap 1 at $\phi = 2$ [μ_1 in Fig. 2(a)] to gap 3 at $\phi = 4$ [μ_3 in Fig. 2(d)]. Figure 4 shows that these two gaps are connected by a continuous region in the (μ, B) plane that contains only edge states. Looking only at the structure of the energy levels the former gap has n_1 states below and the latter has n_2 states below where

$$n_1 = \frac{1}{3}n_L = 2\frac{1}{3}\frac{B}{\phi_0} = 2\frac{1}{3}n_0\frac{\phi}{\phi_0} = 2n_0, \qquad (18)$$

$$n_2 = \frac{3}{4}n_L = 2\frac{3}{4}\frac{B}{\phi_0} = 2\frac{3}{4}n_0 4 = 6n_0. \qquad (19)$$

We have used the proportionality constant $n_0 = (2/\sqrt{3})a^{-2} = 8.02 \times 10^9$ cm^{-2} between B and ϕ. Crucial to the above calculation is the fact that when $\phi = (p/q)\phi_0$ the number of states within a Landau level is evenly distributed between the p subbands. This fact holds within our numerical calculation and can also be demonstrated analytically (see, e.g., Ref. [25], Chap. 12.9, for an argument using the square lattice which applies equally well to triangular lattices). Thus the change in density between these two points is $\Delta n = 4n_0$, while the

change in magnetic field is $\Delta B = n_0\Delta\phi = 2n_0\phi_0$. This calculation gives a Hall conductivity of

$$\sigma_{xy} = e\frac{\Delta n_s}{\Delta B} = e\frac{4n_0}{2n_0\phi_0} = 2\frac{e^2}{h},$$

which agrees with the numerical result in Fig. 4. It also agrees with the results discussed above for Figs. 2(b) and 2(d), obtained by counting edge modes.

VI. QUANTUM PHASE TRANSITIONS DRIVEN BY POTENTIAL STRENGTH

We now move on, in the following two sections (VI and VII), to the central results of this work. In calculations of Hall conductivity (Fig. 4) at different potential strengths we have observed energy gaps whose Chern numbers change as W is increased. Previous numerical work [26] has found changes in the Chern number for a *square* lattice in a magnetic field as coupling between Landau levels is introduced. Topological quantum numbers change when a given energy gap closes and then reopens as a function of some parameter [27]. In our case the parameter which changes the topology is the strength of the potential W. An example of such a transition is given in Fig. 5, which focuses on gap 2 at $\phi/\phi_0 = 4$. In that figure we present a calculation identical to that in Fig. 4 except over the field range $\phi/\phi_0 = 3.5$ to 4.5 and for a larger potential, $W = 0.5, 0.6$, and 0.7 meV. Figure 5(a) corresponds to $W = 0.5$ meV and there is one large continuous gap with Chern number 1 (dark blue). There are also two large disconnected gaps with Chern number 0 (light blue). Increasing the potential to $W = 0.6$ meV in Fig. 5(b) leads to closure of the energy gap with Chern number 1 at $\phi = 4\phi_0$, resulting in four disconnected regions. Increasing W further, to $W = 0.7$ meV, reopens the energy gap at $\phi = 4\phi_0$ in such a way that the Chern number within the gap is now 0. The two light-blue regions from Fig. 5(a) have become connected and the single dark-blue region has become disconnected.

Figures 5(a) and 5(c) are represented schematically in Fig. 6. In this case $\sigma_1 = 0$ and $\sigma_2 = 1$. The top panel in Fig. 6 shows a region of the (μ, B) plane for a value of W before the transition [Fig. 5(a)], while the bottom panel shows the same region after the transition [Fig. 5(c)]. We find that changes in the Chern number are accompanied by changes in the band structure which mirror that sketched in Fig. 6. We also find that, throughout the spectrum, bandgaps with this structure have Chern numbers σ_1 and σ_2, which are separated by multiples of q; $\sigma_2 - \sigma_1 \in q\mathbb{Z}$.

In Fig. 5 $q = 1$ and the statement that $\sigma_2 - \sigma_1 \in q\mathbb{Z} = \mathbb{Z}$ is trivial. There are nontrivial examples, however. The structure sketched in Fig. 6 can be seen elsewhere in the spectrum (Fig. 4) at nonunit values of q. For example, at $\phi/\phi_0 = 2.\dot{3} = 7/3, 2.\dot{6} = 8/3, 3.\dot{3} = 10/3$, and $3.\dot{6} = 11/3$ we have $\sigma_1 = -1$ (green) and $\sigma_2 = 2$ (purple). In each case $q = 3$ and $\sigma_2 - \sigma_1 = 3$. As another example take $\phi/\phi_0 = 2.75 = 11/4$ and $3.75 = 15/4$. Here $q = 4$ and $\sigma_1 = -1$ (green), $\sigma_2 = 3$ (pink), and $\sigma_2 - \sigma_1 = 4 = q$. We have also verified this for $\phi/\phi_0 = 2.4 = 12/5$ and $2.6 = 13/5$ (difficult to see in Fig. 4), where $\sigma_1 = -2$ (yellow) and $\sigma_2 = 3$ (pink), so that $\sigma_2 - \sigma_1 = 5 = q$.
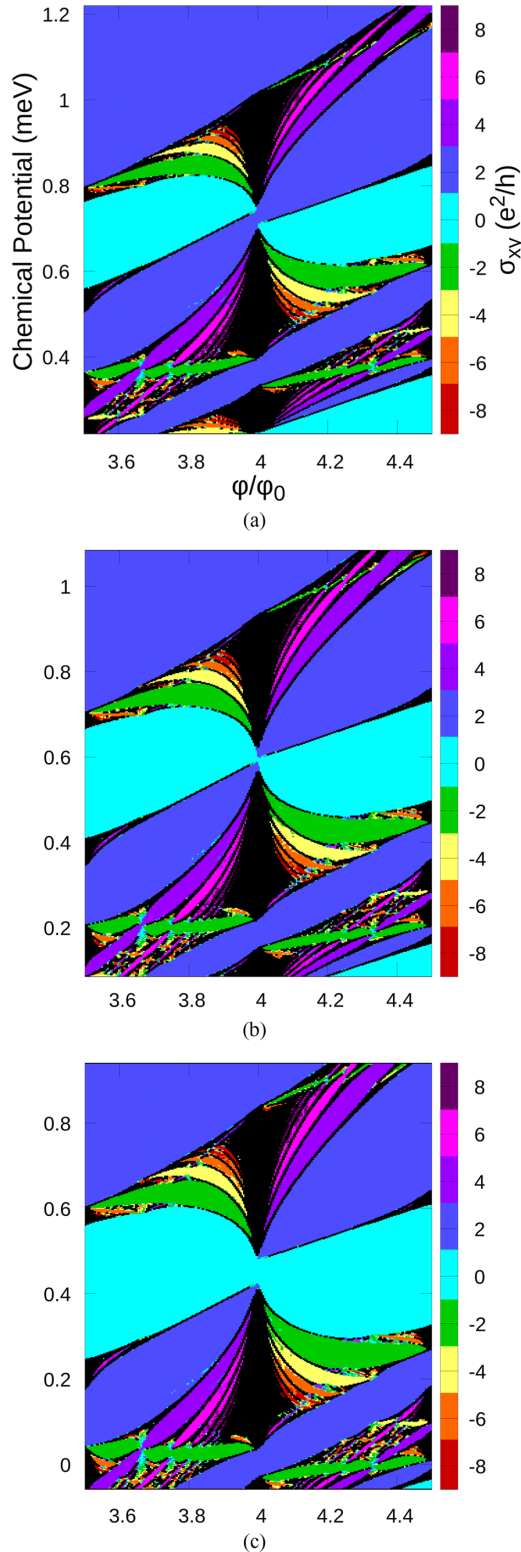
FIG. 5. Maps of σ_{xy} over the (μ, B) plane in the region around gap 2 at $\phi/\phi_0 = 4$. Each plot shows this region at a different potential strength W. (a) $W = 0.5$ meV, (b) $W = 0.6$ meV, and (c) $W = 0.7$ meV.

The Diophantine equation, (17), in Ref. [14] provides some context for this observation. As shown above, for a given energy gap the possible values of ν are separated by multiples
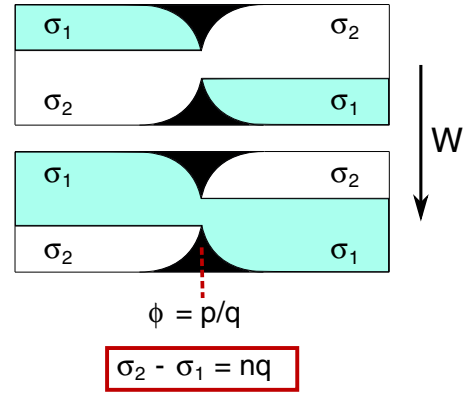

FIG. 6. Schematic of the evolution in band structure on the (μ, B) plane which leads to a change in the Chern number. Black bands represent bulk states and white and blue regions represent connected regions of edge states. As W is increased the central energy gap (at $\phi/\phi_0 = q/p$) closes and then reopens with a different Chern number. Chern numbers in each energy gap are labeled σ_i. We note that if the central gap occurs at a flux $\phi/\phi_0 = p/q$, then the difference in the Chern number between the two gaps shown is an integer multiple of q.

of q. Therefore, if the Chern number were to change as in Fig. 6, then the original value, σ_2, would have to be separated from the final value, σ_1, by a multiple of q. Seeing only the initial or the final configuration depicted in Fig. 6 (i.e., with $\sigma_2 - \sigma_1 = nq$) suggests that a transition is possible.

Characterizing the dependence on the modulation strength of experimentally relevant parameters is useful for understanding actual AG devices. We have computed Hall conductivity values which depend not only on the lattice symmetry but also on the height of the superlattice potential. This could provide a means of experimentally determining the superlattice strength in real devices. As demonstrated in Ref. [11] the presence of a second set of Dirac cones is directly dependent on the potential strength. In principle, it would be possible to measure the value of W at $B > 0$. One could then make a statement about the band structure at $B = 0$.

VII. CURRENT STREAMS IN BULK

In this section we present our results for the spatial distribution of the current density. We consider the current density only for chemical potentials within bulk bandgaps. The central message is that extended current streams exist in the sample's bulk whenever μ is within a bulk bandgap.

Figure 7 shows our results for the current density. The left column in Fig. 7 presents color maps of the y component of the current density in bulk bandgaps μ_1, μ_2, and μ_3 for $W = 0.4$ meV and $\phi = 3\phi_0$ [as in Fig. 2(b)]. We stress, again, that the chemical potentials are within the bandgap. Zero-current contours are shown in light blue. We have labeled each antidot center with a white circle and have placed the boundaries of the plot at the walls of the confining potential, Eq. (8)]. Each plot in the right column in Fig. 7 shows a horizontal cut of the color map to its left taken along $y = 0.5a$. All calculations we performed with $L_x = 10a = 1.2$ μm.

Our first observation is that the current in the bulk of the sample is arranged into a set of extended streams which pass
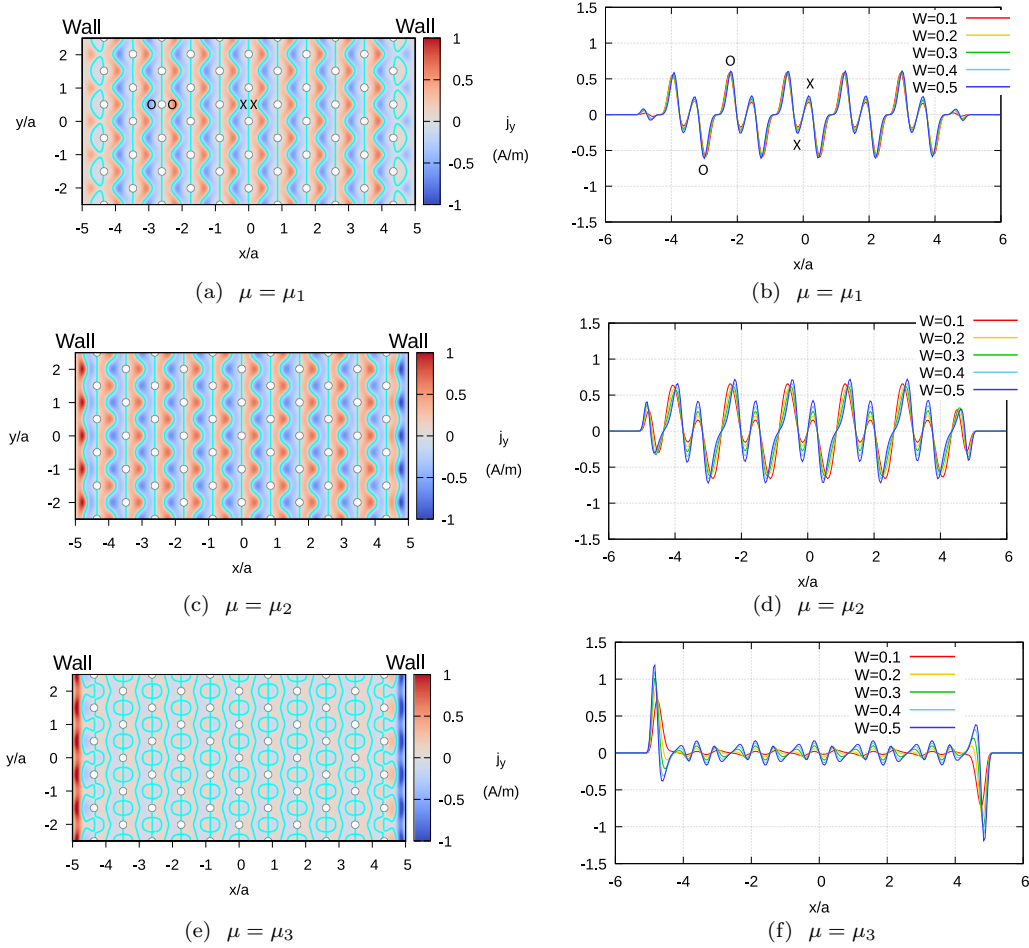
FIG. 7. Overview of computed j_y data at each value of the chemical potential shown in Fig. 2(b). The first column contains color maps of $j_y(x, y)$ at $W = 0.4$ meV, $a = 120$ nm, and $\phi/\phi_0 = 3$ for (a) $\mu = \mu_1$, (c) $\mu = \mu_2$, and (e) $\mu = \mu_3$ [see Fig. 2(b)]. Solid blue lines indicate the points for which $j_y(x, y) = 0$ and white circles indicate antidot lattice sites. Each plot in the second column [(b), (d), (f)] shows a cut of the data to its left taken at $y = 0.5a$ [i.e., $j_y(x, 0.5a)$]. In addition, we include the data for $W = 0.1, 0.2, 0.3$, and 0.5 meV. The labels O and X in (a) and (b) indicate the circulating and extended parts of the current, respectively. In each calculation we fix $L_x = 10a = 1.2$ μm.

through the entire sample. This follows from the fact that zero-current contours form open regions which connect the top and bottom of the plotted area and that the current is periodic along the y direction. Each stream that carries current along a particular direction is balanced by a stream carrying current along the opposite direction. We observe that these streams are present in every bulk bandgap at all magnetic field values tested. As discussed below, the magnitude of the extended streams of current is reduced when moving from a fractionally filled Landau level to a fully filled Landau level.

Besides the extended currents there is a second component which circulates around antidots. In Figs. 7(a) and 7(c) this current is counterclockwise. We have verified this interpretation by looking at the x component of the current. These two components are labeled in Fig. 7(b). An example of extended streams in this plot are the two peaks centered around $x = 0$ and labeled X. And an example of circulating currents is the two larger peaks centered at $x = -3\sqrt{3}a/2 \approx -2.6a$ and labeled O. This value of x corresponds to an antidot center.

The current profile evolves as the chemical potential is moved through a Landau level. A current distribution, shown

in Fig. 7(b), is established when the chemical potential is in the first gap, $\mu = \mu_1$ in Fig. 2(b). When μ increases to μ_2 the amplitude of the streams increases slightly [Fig. 7(d)]. A further increase in μ, to μ_3, so that all states within the Landau level are occupied, leads to an overall reduction in the current density, both the circulating and the extended parts [Fig. 7(f)]. This evolution between μ_2 and μ_3 applies at all the magnetic field values tested. Moving the chemical potential across the final subband always reduces the amplitude to a fraction of its original value. In spite of this reduction, both the streams and the circulating currents are nonzero even when the chemical potential is between Landau levels. For large potentials the remaining bulk current amplitude is not negligible compared to the edge current.

Scaling of currents with potential strength

The bulk distribution of the current density is dependent on the potential strength W. In Figs. 7(b), 7(d) and 7(f) we consider the current density at $W = 0.1, 0.2, 0.3, 0.4$, and 0.5 meV.

The bulk current density scales with W in different ways depending on the value of μ. At $\mu = \mu_3$ [Fig. 7(f)], corresponding to a fully filled Landau level, the entire bulk current density scales roughly in proportion to W. This is consistent with the bulk current density being 0 in the $W \to 0$ limit. This proportionality was observed at all magnetic fields tested when μ covers the entire Landau level. For values of μ inside a Landau level but between two magnetic bulk subbands, scaling is more complicated. In Fig. 7(b) ($\mu = \mu_1$) both the extended and the circulating parts of the bulk current density are independent of W. When μ is increased to μ_2 [Fig. 7(d)] the circulating part of the current density remains independent of W while the extended streams scale weakly with W. At other magnetic field strengths the scaling of the bulk current density with W follows similar patterns.

In the limit $W \to 0$ the bandwidth of the Landau level goes to 0 and μ_1, μ_2, and μ_3 approach the same value. It then becomes unclear how to define a fractional filling of the Landau level. For small (but finite) W, however, we observe little or no scaling in the bulk current at μ_1 and in the circulating part of the current at μ_2. Of course, at very small W disorder wins over the periodic potential and our analysis becomes invalid.

We have shown that fully filled bulk bands of the Hofstadter butterfly lead to a current density which contains extended streams of current. The amplitude of these streams scales with the height of the lattice potential.

It is well known that in the conventional quantum Hall effect there are bulk percolation currents when the chemical potential is within the bulk band formed by a disorder-broadened Landau level (Ref. [25], Chap. 12.7). The streams that we discuss here have some analogy with this effect. Nevertheless, the two effects are very different. Here we highlight the two most important differences. (i) Our streams exist when the chemical potential is in the gaps between bulk subbands. On the other hand, percolation currents in the conventional quantum Hall effect exist when the chemical potential is within a bulk band. (ii) The streams exist even if the chemical potential is in the gap between Landau levels. The amplitude of the stream current in this case is proportional to the potential amplitude. There is no analogy to this in the conventional case.

To avoid misunderstanding we stress that the total current that we observe is 0 since all of the streams compensate each other. Thus, in standard terminal measurements, the streams cannot be observed. The equilibrium and nonequilibrium current streams in the bulk can be detected, however, via the magnetic field they produce using nitrogen-vacancy-center magnetometry [28,29]. We estimate magnetic fields of the order of 0.1 mG at 100 nm above the 2DEG, which is well within the sensitivity of this method. The factor that complicates the measurement is the external magnetic field: one would need to detect a 0.1-mG signal in the presence of a background field of the order of 1 T.

VIII. CONCLUSIONS

We have analyzed the dynamics of electrons in a triangular lattice of antidots in the presence of a strong magnetic field. The periodic triangular potential is "moderately strong." This means that the amplitude is comparable to that necessary to produce artificial graphene. There are two key theoretical findings in the work. (i) Proper variation of the potential amplitude drives topological quantum phase transitions between states with different Chern numbers. (ii) The superlattice generates bulk current streams for values of the chemical potential within a bulk bandgap. The effect cannot be observed in standard terminal measurements, but it can be observed using nitrogen-vacancy-center magnetometry.

Besides the theoretical findings, our work could be of use in experimental studies of AG. The presence of Dirac cones in antidot AG depends on the strength of the potential modulation. Our results allow for calibration of the potential modulation strength via observation of the quantum Hall plateaus.

[1] L. Du, S. Wang, D. Scarabelli, L. N. Pfeiffer, K. W. West, S. Fallahi, G. C. Gardner, M. J. Manfra, V. Pellegrini, S. J. Wind *et al.*, Nat. Commun. **9**, 3299 (2018).

[2] S. Wang, D. Scarabelli, L. Du, Y. Y. Kuznetsova, L. N. Pfeiffer, K. W. West, G. C. Gardner, M. J. Manfra, V. Pellegrini, S. J. Wind *et al.*, Nat. Nanotechnol. **13**, 29 (2018).

[3] L. C. Post, T. Xu, N. A. F. Vergel, A. Tadjine, Y. Lambert, F. Vaurette, D. Yarekha, L. Desplanque, D. Stiévenard, X. Wallart *et al.*, Nanotechnology **30**, 155301 (2019).

[4] M. C. Geisler, J. H. Smet, V. Umansky, K. von Klitzing, B. Naundorf, R. Ketzmerick, and H. Schweizer, Phys. Rev. Lett. **92**, 256801 (2004).

[5] Y. Iye, M. Ueki, A. Endo, and S. Katsumoto, J. Phys. Soc. Jpn. **73**, 3370 (2004).

[6] C. Forsythe, X. Zhou, K. Watanabe, T. Taniguchi, A. Pasupathy, P. Moon, M. Koshino, P. Kim, and C. R. Dean, Nat. Nanotechnol. **13**, 566 (2018).

[7] B. S. Jessen, L. Gammelgaard, M. R. Thomsen, D. M. A. Mackenzie, J. D. Thomsen, J. M. Caridad, E. Duegaard, K. Watanabe, T. Taniguchi, T. J. Booth *et al.*, Nat. Nanotechnol. **14**, 340 (2019).

[8] G. Jotzu, M. Messer, R. Desbuquois, M. Lebrat, T. Uehlinger, D. Greif, and T. Esslinger, Nature **515**, 237 (2014).

[9] T. Uehlinger, G. Jotzu, M. Messer, D. Greif, W. Hofstetter, U. Bissbort, and T. Esslinger, Phys. Rev. Lett. **111**, 185307 (2013).

[10] M. Polini, F. Guinea, M. Lewenstein, H. C. Manoharan, and V. Pellegrini, Nat. Nanotechnol. **8**, 625 (2013).

[11] O. A. Tkachenko, V. A. Tkachenko, I. S. Terekhov, and O. P. Sushkov, 2D Mater. **2**, 014010 (2015).

[12] D. R. Hofstadter, Phys. Rev. B **14**, 2239 (1976).

[13] F. H. Claro and G. H. Wannier, Phys. Rev. B **19**, 6068 (1979).

[14] D. J. Thouless, M. Kohmoto, M. P. Nightingale, and M. den Nijs, Phys. Rev. Lett. **49**, 405 (1982).

[15] A. H. MacDonald, Phys. Rev. B **29**, 3057 (1984).

[16] R. R. Gerhardts, D. Weiss, and K. v. Klitzing, Phys. Rev. Lett. **62**, 1173 (1989).

[17] D. Q. Wang, D. Reuter, A. D. Wieck, A. R. Hamilton, and O. Klochan, unpublished (2020).

[18] Please note that this definition of the flux quantum differs from the superconducting flux quantum $h/2e$.

[19] B. I. Halperin, Phys. Rev. B **25**, 2185 (1982).

[20] P. Streda, J. Phys. C **15**, L717 (1982).

[21] P. Streda, J. Phys. C **15**, L1299 (1982).

[22] A. H. MacDonald, Phys. Rev. B **29**, 6563 (1984).

[23] We compute the Hall conductivity via Eq. (13). Numerical differentiation is performed using a centered difference with step size $d\phi = 2 \times 10^{-3} \phi_0$.

[24] The density of states at E is computed by counting the number of energy levels which fall into the range $E + dE$. We use $dE = 1 \times 10^{-3}$ meV.

[25] S. M. Girvin and K. Yang, *Modern Condensed Matter Physics* (Cambridge University Press, Cambridge, UK, 2019).

[26] D. Springsguth, R. Ketzmerick, and T. Geisel, Phys. Rev. B **56**, 2036 (1997).

[27] C. L. Kane and E. J. Mele, Phys. Rev. Lett. **95**, 226801 (2005).

[28] J. M. Taylor, P. Cappellaro, L. Childress, L. Jiang, D. Budker, P. R. Hemmer, A. Yacoby, R. Walsworth, and M. D. Lukin, Nat. Phys. **4**, 810 (2008).

[29] S. Hong, M. S. Grinolds, L. M. Pham, D. L. Sage, L. Luan, R. L. Walsworth, and A. Yacoby, MRS Bull. **38**, 155 (2013).